ARTICLES
https://doi.org/10.1038/s41561-020-0640-z
nature geoscience

Active crustal differentiation beneath the Rio Grande Rift

Jacob H. Cipar[1]✉, Joshua M. Garber[1], Andrew R. C. Kylander-Clark[2] and Andrew J. Smye[1]✉

Silicon-rich continental crust is unique to Earth. Partial melting during high- to ultrahigh-temperature metamorphism (700 °C to >900 °C) promotes the long-term stability of this crust because it redistributes key elements between the crust and mantle and ultimately produces cooler, more-differentiated continents. Granulites—rocks formerly at high- to ultrahigh-temperature conditions—preserve a record of the stabilization of Earth's continents, but the tectonic mechanisms that drive granulite formation are enigmatic. Here we present an analysis of lower-crustal xenoliths from the Rio Grande Rift—a nascent zone of extension in the southwestern United States. Uranium–lead geo- and thermochronology combined with thermobarometric modelling show that the lower 10 km of the crust currently resides at granulite-facies conditions, with the lowermost 2 km at ultrahigh-temperature conditions. Crust and mantle xenoliths define a continuous pressure-and-temperature array, indicating that a thin lithospheric mantle lid mediates elevated conductive heat transfer into the crust. These findings establish a direct link among ultrahigh-temperature metamorphism, collapse of the Laramide orogen and lithospheric mantle attenuation. Other indicators of modern ultrahigh-temperature metamorphism are consistent with these conditions prevailing over thousands of square kilometres across the US–Mexico Basin and Range province. Similarities between the pressure-and-temperature path from the Rio Grande lower crust and those from exhumed granulite terranes imply that post-thickening lithospheric extension is a primary mechanism to differentiate Earth's continental crust.

After its formation at volcanic arcs, nascent continental crust undergoes a suite of differentiation processes that stabilize it against long-term mantle convection. These processes include the loss of dense, mafic cumulates to the mantle (delamination[1]), the recycling of felsic components from the upper to the lower crust (relamination[2]) and the transfer of heat-producing elements from the lower to upper crust[3]. Partial melting and (ultra) high-temperature ((U)HT) metamorphism facilitate this differentiation, but the tectonic environments at which these processes occur are unclear[4]. Granulites—rocks metamorphosed at high-temperature, medium-pressure conditions (>700 °C; 4–15 kbar) that are above the wet solidus of most silicic crust—are composed of relatively dense residua from which silicic melt has been extracted and are associated with most major crust-forming and reworking episodes throughout geological history[5]. Because they represent the residues of crustal melting, granulitization events preserve a record of the differentiation of Earth's continents—a process that can result in its long-term rheological stabilization against mantle convection (for example, ref. [3]). Despite extensive study of ancient granulite terranes—often hampered by pervasive recrystallization and diffusive modification during exhumation or later tectonism[6]—the tectonic processes responsible for granulite-facies metamorphism are still debated; a commonly held view is that the cores of large collisional orogens, such as the India–Asia collision, are the most common spawning grounds for granulites[5,7]. Less attention has been paid to extensional settings as culprits for granulite formation[8], although many granulite occurrences have isobarically cooled from peak temperature (T) (ref. [9]) and are dominated by subhorizontal rock fabrics—observations typically expected of rocks from extensional tectonic settings[10]. Here, we show that young lower-crustal xenoliths from the southern Rio Grande Rift (RGR), southwestern United States, preserve a record of ongoing granulite formation, thus firmly linking active extensional tectonism with UHT metamorphism, differentiation and plate-scale strengthening of continental crust.

The RGR is an active continental rift extending at a rate of ~1 mm yr^{-1} (ref. [11]); the axial zone of the rift broadens over the course of its ~1,000 km length, from Leadville, Colorado, to south of El Paso, Texas, where it becomes indistinguishable from the Basin and Range physiographic province (Fig. 1). Sedimentary, magmatic and structural data suggest a complex tectonic history spanning a transition from late-Laramide compression (60–40 Ma) to discrete episodes of extension and volcanism between ~35–20 Ma and from ~10 Ma to the present[12]. Regionally elevated surface heat flow (90–110 mW m^{-2}) (ref. [13]), seismically derived Moho temperature estimates >800 °C (ref. [14]) and slow P- and S-wave velocities at depths as shallow as 45 km (ref. [15]) suggest extreme temperatures and the possible presence of melt in the lower crust and upper mantle beneath the RGR. These regionally high temperatures are interpreted to be the result of removal of mantle lithosphere beneath the rift because (1) the crust has undergone minor extension (<25%) since the mid-Oligocene[16] and remains ~32 km thick beneath the southernmost rift[17]; (2) a regional-scale large-wavelength gravity low is associated with low upper-mantle seismic velocities beneath the rift[12]; (3) ultramafic xenoliths with asthenospheric isotope signatures were erupted from ~45 km beneath the southern RGR[18]; (4) dynamic uplift is recorded in subsidence histories from syn-rift sedimentary successions, interpreted to record the loss of a lithospheric mantle root[19]; and (5) mantle P- and S-wave anomalies imaged by seismic tomography are interpreted to record ongoing mantle convection between ~55 and 90 km (ref. [15]). The presence of partial melt in the middle and lower crust is also supported by magnetotelluric data showing anomalously high conductivity at 10–20 km depth along the length of the rift, although this anomaly may also represent a

[1]Department of Geosciences, The Pennsylvania State University, University Park, PA, USA. [2]Department of Earth Science, University of California, Santa Barbara, CA, USA. ✉e-mail: jhc5220@psu.edu; smye@psu.edu

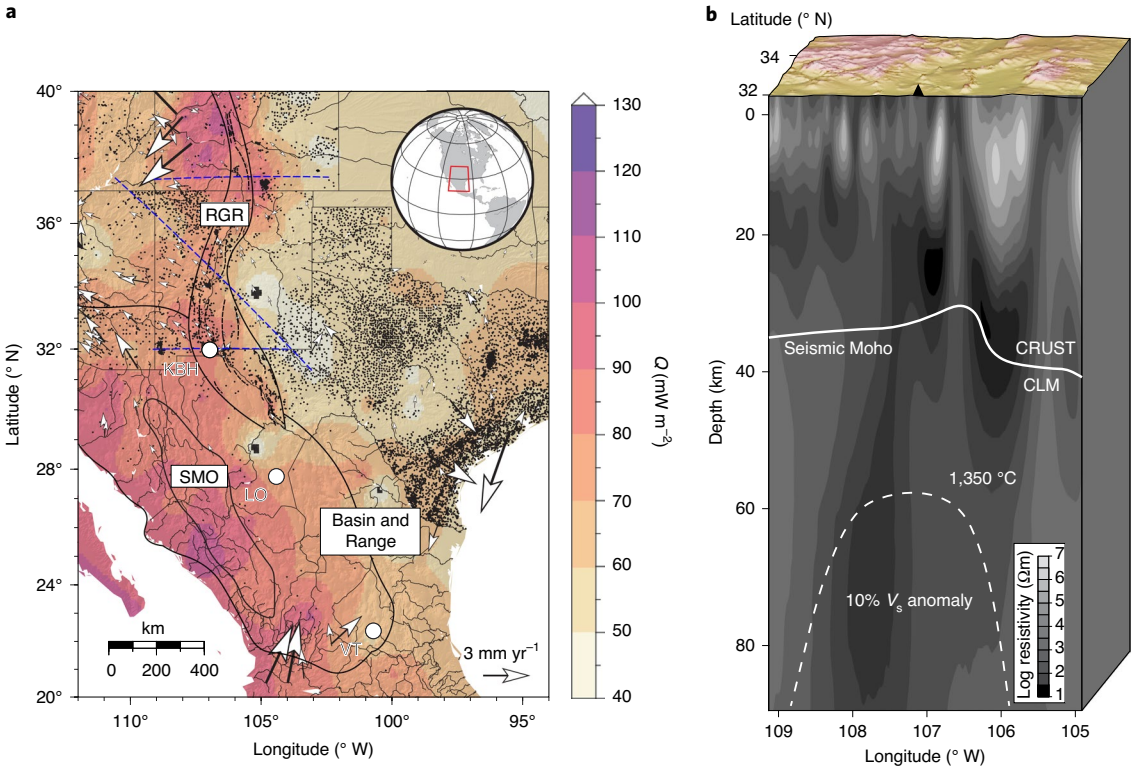

Fig. 1 | Map and cross section summarizing RGR geologic and geophysical data. a, Heat flow and topography for the RGR system in the United States and northern Mexico. Arrows represent GPS velocity vectors relative to stable North America (UNAVCO, PBO NAM14 dataset); dashed blue lines represent (in order from north to south) the locations of the teleseismic CREST[50] and LA RISTRA[15] experiments and an electrical resistivity profile[20]. Black dots represent heat-flow measurement locations from conventional heat-flow measurements and oil- and gas-well bottom-hole temperatures[13,51]. Black lines show faults (dashed) and boundaries between physiographic provinces (solid) after ref. [12]. Quaternary volcanic centres known to contain similar lower-crustal xenoliths are shown as white dots. *Q*, surface heat flow; LO, La Olivina; VT, Ventura Volcanic Field; SMO, Sierra Madre Occidental. **b**, Rift-perpendicular electrical resistivity model near KBH[20] (along southernmost profile in **a**) showing Moho beneath KBH[17] and depth of 10% shear wave velocity (V_s) anomaly[43]. CLM, continental lithospheric mantle.

saline-rich fluid[20]. Assuming a steady-state conductive geotherm, the heat-flow data imply that the deep crust beneath the RGR is currently residing at HT–UHT conditions and that attainment of these conditions is contemporaneous with convective removal of lithospheric mantle. However, direct samples of deep RGR crust are required to determine whether granulite formation is an active or extinct process.

Kilbourne Hole maar (KBH), known for its abundant and diverse xenolith population, erupted ~20 Ka and is situated in the Potrillo Volcanic Field west of El Paso[21,22]. Xenoliths are derived from both crust and mantle lithologies, with the crustal suite dominated by metapelites. Published pressure and temperature (*PT*) estimates for KBH granulite xenoliths span ~6–9 kbar and ~860–1,000 °C (refs. [21,23,24]), but it is uncertain whether these *PT* estimates represent an earlier peak metamorphic event, the modern geotherm or conditions associated with magmatic heating upon eruption. Early studies argued that these xenoliths were in thermodynamic equilibrium in the lower crust just before eruption[21], but more-recent petrologic and thermal modelling studies have proposed that KBH granulite metamorphism occurred earlier (~30 Ma) and that the lithosphere has subsequently cooled since the late Oligocene[24].

Granulite xenoliths from the crust–mantle boundary

We performed a systematic petrochronological investigation of a suite of metapelitic and mafic granulite xenoliths from KBH to constrain the *PTt* (where *t* is time) evolution of the RGR lower crust. We focused on seven metasedimentary granulite xenoliths ('group 1' granulites of ref. [21]) and two mafic granulites (see Methods for petrographic descriptions); the metapelites are characterized by residual assemblages with partly unmixed, former ternary feldspar, as well as quartz, garnet, sillimanite, rutile, ilmenite and zircon (Fig. 2; the petrography of these rocks has been previously described in the literature[21,25]). The co-occurrence of these minerals makes these samples ideal for both novel and conventional petrologic techniques. Garnet is notably devoid of major element zoning. Embayed grain boundaries, centimetre-scale quartz-feldspar leucosomes and the absence of hydrous mineral phases (Fig. 2a) are consistent with the presence (or former presence) of melt in these rocks immediately before extraction from the lower crust. Likewise, elevated lutetium/hafnium whole-rock ratios[26] and trace-element mass balance constraints[27] are permissible with the extraction of 20–30% partial melt from the KBH metapelites. Estimated *PT* conditions recorded by the crustal xenoliths were calculated from the intersections among multiple-phase equilibria: the titanium- (Ti) in-quartz[28] and zirconium- (Zr) in-rutile[29] thermometers and the GASP/GRAIL barometers[30] (further calculation details are provided in the Methods). Calculated pressures were converted to depths using the seismically derived density structure of the crust at KBH[17]. Computed metapelite *PT* conditions are 8–10 kbar (29–36 km) and 870–960 °C and agree with those determined with *PT* pseudosections (Extended Data Fig. 1). These depth estimates further overlap with the Moho beneath KBH (~32 km) (ref. [17]). To assess the degree of continuity in *PT* conditions between lower-crustal and mantle xenoliths from KBH, *PT* pseudosections were constructed

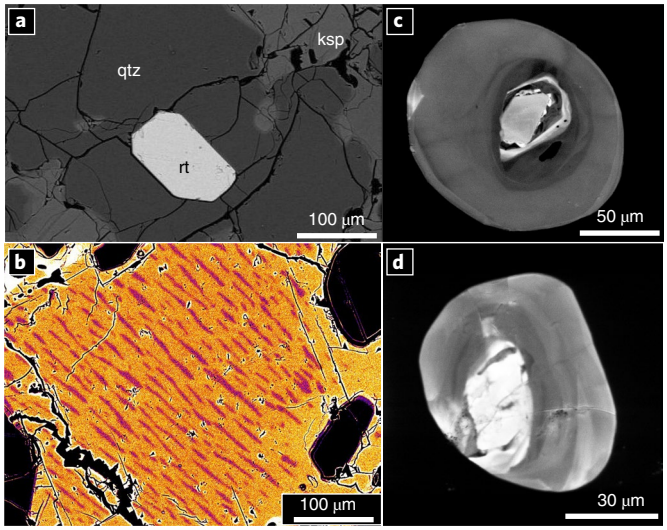

Fig. 2 | Metapelitic xenolith petrology. a, Back-scattered electron image of rutile- (rt) bearing migmatite with embayed grain boundaries between quartz (qtz) and K-feldspar (ksp), indicative of former presence of melt (sample JC18KH28). **b**, False-coloured back-scattered electron image of plagioclase exsolution lamellae in K-feldspar host crystal (sample JC18KH28). **c**,**d**, Zircon CL images, samples JC18KH28 (**c**) and JC18KH16 (**d**).

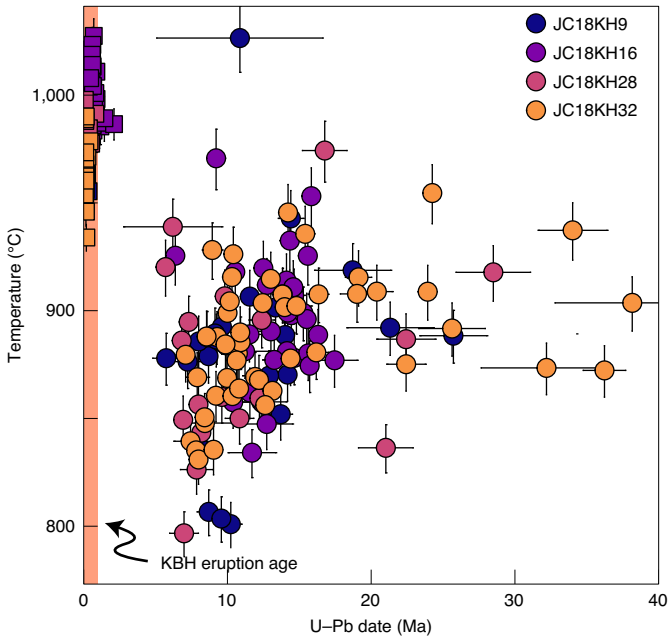

Fig. 3 | Zircon and rutile temperature–time data. Data represent U–Pb zircon (circles) and rutile (squares) dates and associated Ti-in-zircon and Zr-in-rutile thermometry. Zircon age errors are 2σ. Orange band represents time of xenolith extraction[22].

for three spinel lherzolites (Methods). Equilibration temperatures were calculated from the average of the sodium (Na) and iron–magnesium (Fe–Mg) exchange thermometers between clinopyroxene and orthopyroxene[31]. Bounds to the equilibration pressures for KBH mantle xenoliths were estimated on the basis of the coexistence of spinel, orthopyroxene, clinopyroxene and olivine and the Moho[17]. Calculated *PT* conditions for KBH lherzolites KH-11, KH-29 and KLB-1 are 970–1,040 °C and 10–13 kbar (Extended Data Fig. 2), slightly higher than the *PT* conditions derived from the crustal xenoliths. The *PT* data are consistent with the interpretation that the lower-crustal and spinel lherzolite xenoliths sample a ≤10-km-depth interval across the crust–mantle boundary.

Modern-day HT–UHT metamorphism

To link *PT* conditions and time, zircon and rutile mineral separates were analysed for U–Pb isotopes and trace elements by laser-ablation inductively coupled plasma mass spectrometry (Methods). Zircon grains exhibit complex internal zoning (Fig. 2c,d), with multiple light to dark rounded rims observable in cathodoluminescence (CL) images. U–Pb dates span ~1,500 Myr, with the greatest density of dates at ~20–10 Ma. The youngest zircon rim dates (~5 Ma) have Ti contents ~50–70 ppm, corresponding to 920–970 °C at 10 kbar (ref. [32]) (Fig. 3). Ti-in-zircon thermometry from older zircon zones further demonstrates that the lower crust beneath KBH has resided at >800 °C for at least the past 20 Myr (Fig. 3). Zircon from mafic granulites further exhibit a pronounced change in heavy rare-earth element (HREE) patterns at 20–30 Ma (Extended Data Fig. 3): zones with U–Pb dates ≥20 Ma are characterized by flatter HREE profiles, implying the former presence of garnet, whereas younger zones have steeper HREE profiles, consistent with the observed garnet-absent mineralogy of the samples. Rutile U–Pb dates are effectively zero-age despite non-zero U concentrations (~3–31 ppm), and associated Zr-in-rutile concentrations range from ~2,500 to ~8,500 ppm (~853–1,017 °C at 10 kbar (ref. [29])). Exsolved lamellae of plagioclase in potassium (K) feldspar provide an additional temperature constraint; calculated temperatures of feldspar miscibility are similar to the zircon and rutile data (870–1,000 °C; Extended Data Fig. 4). Although the thermobarometric results are consistent among all analysed minerals, our best absolute age constraint on these *PT* conditions is based on the absence of measurable radiogenic Pb in rutile. This signature can be interpreted either as recording recent rutile growth at UHT conditions or as protracted xenolith residence at temperatures above those required for rutile U–Pb closure (~620 °C (ref. [33])). Regardless of the preferred interpretation, zero-age rutile establishes minimum pre-eruptive temperatures of 620 °C. At and above these minimum temperatures, chemical equilibrium in major phases will be achieved rapidly. Hypothetically, if the *PT* conditions recorded by major and trace-element geothermometers presented in the preceding represent an ancient HT event and the lower crust has since cooled, there would be observable garnet zoning; major cation diffusivities in garnet exceed 100 μm over million-year timescales at such temperatures[34]. Garnets in KBH metapelites are not zoned, demonstrating that the thermobarometric results presented in the preceding represent pre-eruptive *PT*. This is also true for feldspar: conductive cooling of the samples in the lower crust would have allowed appreciable Na–K diffusion, leading to disequilibrium between plagioclase and alkali-feldspar solvus temperatures[35], which was not observed. Finally, simple numerical models of heating associated with recent magmatic entrainment and eruption show that neither was a causal heat source for the observed metamorphism; length scales of major and minor element diffusion during magmatic heating related to eruption of KBH xenoliths (~3 yr) (ref. [36]) are negligible (Extended Data Fig. 5).

Because the heat conduction length scale through crustal rocks is over 20 kyr (time since eruption) is ≤1 km (Extended Data Fig. 6), we interpret the xenolith *PT* estimates to represent the present-day thermal structure of the RGR lower crust. Combined with local geophysical observations, these data tightly constrain the modern thermal structure of the southern RGR. Additional temperature–depth (*T*–*z*) estimates for the shallow crust can be calculated from conventional heat-flow measurements and oil- and gas-well bottom-hole temperatures[13], and the depth to the magnetite Curie temperature (~550 °C at 15 km in the southern RGR) can be inferred from aeromagnetic data[37]. The composite geotherm (Fig. 4a) shows that the

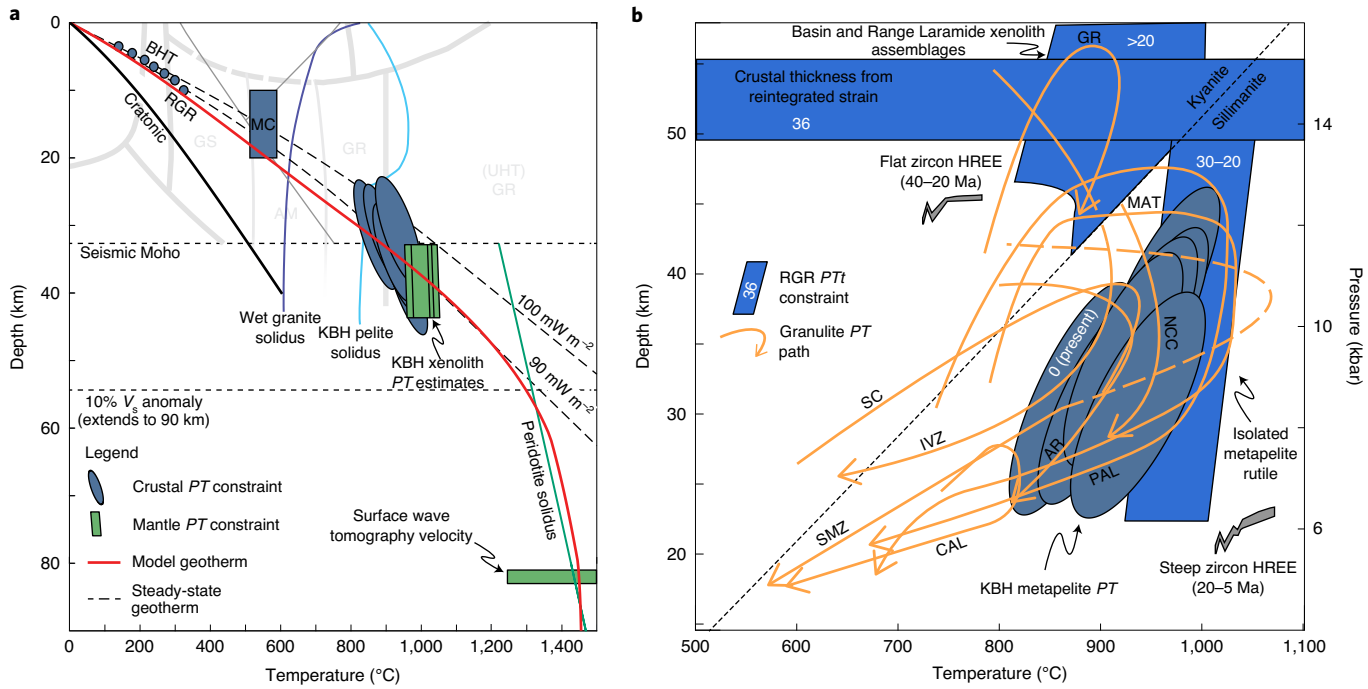

Fig. 4 | Modern-day lithospheric geotherm beneath KBH and comparison with ancient granulite terranes. a, Temperature–depth constraints are from metapelite thermobarometry (blue ellipses), depth to the magnetite Curie isotherm (MC; blue rectangle) and extrapolation from near-surface measurements (BHT; blue circles). Mantle depth and temperature estimates (green rectangles) are from two-pyroxene thermometry and the seismically defined Moho beneath KBH[17], as well as temperature inversions from surface wave tomography velocities[52]. Also shown are the dry peridotite solidus[53], 0.4 °C km^{-1} mantle adiabat, wet granite solidus[54], metamorphic facies grid and aluminosilicate phase diagram. Steady-state geotherms calculated for the observed range of surface heat flows near KBH are shown as black dashed lines; the solid red line represents model geotherm calculated for 30 Myr of depth-dependent thinning (crustal and mantle thinning factors: 1.25 and 6, respectively) and the black line represents stable cratonic geotherm using adjacent Great Plains surface heat flow and crustal thickness[55]. **b**, Comparison of RGR *PTt* constraints with *PT* paths derived from exhumed granulite terranes (orange arrows; see Supplementary Information for full reference list). Light-blue polygons represent >20 Ma *PT* constraints from the RGR (ages are superimposed); darker ellipses correspond to modern *PT* constraints. Zircon REE patterns (embedded) from KBH mafic granulites show evolution from garnet-present to garnet-absent conditions. Also shown is the aluminosilicate phase diagram. IVZ, Ivrea Zone, Italy; MAT, Rauer Group, East Antarctica; PAL, Palni Hills, south India; SMZ, Southern Marginal Zone, Limpopo Complex, South Africa; GR, central Grenville; AR, Arunta Complex, central Australia; CAL, southern Calabria, Italy; NCC, North China Craton.

lower ~10 km of crust beneath KBH is currently experiencing *PT* conditions associated with granulite-facies metamorphism, with the lowermost ~2 km undergoing UHT metamorphism.

We note that the physiographic expression of the RGR rift axis spans >1,000 km and that elevated heat flow (>80 mW m^{-2}; Fig. 1) and reduced mantle lithosphere thickness continue broadly uninterrupted into and across the US–Mexico Basin and Range province over thousands of kilometres[13,38]. Combined with the presence of near-identical lower-crustal xenoliths along this axis[39,40] (Fig. 1), these observations support the notion that a granulite terrane, with dimensions similar to the largest exhumed HT–UHT terranes[41], is forming in the lower crust beneath the RGR and much of northern Mexico today.

A key implication of the reported thermal structure is that a felsic silicate melt phase probably resides in the modern lower crust of the southern RGR. Partially molten lower crust is supported by (1) low electrical resistivity anomalies coincident with xenolith extraction depths (Fig. 1b)[20]; (2) the lack of hydrous mineral phases in KBH xenoliths; (3) the documented occurrence of silicate melt-filled cracks in KBH granulites[21]; and (4) computed melt abundances in KBH pelites (Extended Data Fig. 1). Moho temperatures of ~900 °C and the presence of partial melt imply that the effective viscosity of lower crust beneath KBH is low enough for flow to occur in response to tectonic stresses[42]. Flow of the lower crust can account for the observation that lower-crustal deformation in the Rio Grande is distributed over a width four times as large as the upper crust, as well as the flat Moho documented beneath the central portion of the rift[43].

Mantle thinning as a mechanism to form granulites

Steady-state conductive geotherms assuming uniform distributions of heat-producing elements and surface heat-flow values comparable to those measured near KBH (90–110 mW m^{-2}; Fig. 1) are remarkably similar to the composite geotherm (Fig. 4). This implies that the present thermal structure of the crust approximates conductive thermal equilibrium and that the observed elevated surface heat flow—while it does not preclude magmatic underplating—need not be supported by advected magmatic heat. To constrain potential heating mechanisms, we performed thermal-kinematic calculations (Methods) for two tectonic scenarios applicable to the RGR: (1) instantaneous removal of mantle lithosphere at the initiation of RGR extension (~30 Myr (ref. [12])) followed by continuous replenishment of asthenospheric heat and (2) continuous depth-dependent extension since 30 Ma, in which the lithospheric mantle is thinned at a rate that exceeds that of crustal thinning. Both mechanisms produce geotherms notably similar to the observed thermal structure (Extended Data Fig. 7); the modern-day geotherm for the depth-dependent thinning scenario is plotted on Fig. 4a. These calculations support the interpretation that the primary heating mechanism for HT–UHT metamorphism and attendant partial melting is lithospheric thinning but also demonstrate that the modern-day thermal structure of the southern RGR may be the result of either

protracted or rapid removal of the mantle lithosphere. Both tectonic scenarios are consistent with granulite-facies conditions affecting the lower crust of the RGR for tens of millions of years, as recorded by elevated Ti-in-zircon temperatures throughout the history of the RGR (Fig. 3).

Following late-Laramide compression (~60–40 Ma) and before the onset of extension (~35 Ma), the southern RGR crust was between 40 and 50 km thick[44], accounting for the garnet-present zircon HREE pattern observed in KBH mafic granulites. Within ~20 Myr of its cessation, crustal thickening was succeeded by lithospheric removal, crustal thinning and, as shown in this study, heating of the lower crust to granulite-facies conditions. This sequence of tectonic events can be attributed to the dissipation of gravitational potential energy stored within orogenic crust—a key phase in the structural evolution of active and ancient mountain belts, including, among others, the Tibetan Plateau[45], the Betic-Rif orogen[46] and the Variscan belt of Europe[47]. Crustal *PT* paths for this mechanism are characterized by heating during decompression (Extended Data Fig. 8), analogous to *PT* paths derived from many exhumed HT–UHT terranes[48,49] (Fig. 4b and Extended Data Fig. 8). The data presented here thus imply that gravitational collapse of thickened lithosphere is an active, plate-scale process to form granulites, attain UHT conditions and chemically differentiate the continental crust.

Online content

Any methods, additional references, Nature Research reporting summaries, source data, extended data, supplementary information, acknowledgements, peer review information; details of author contributions and competing interests; and statements of data and code availability are available at https://doi.org/10.1038/s41561-020-0640-z.

Received: 13 December 2019; Accepted: 24 August 2020;
Published online: 12 October 2020

References

1. Kay, R. W. & Kay, S. M. Delamination and delamination magmatism. *Tectonophysics* **219**, 177–189 (1993).
2. Hacker, B. R., Kelemen, P. B. & Behn, M. D. Differentiation of the continental crust by relamination. *Earth. Planet. Sci. Lett.* **307**, 501–516 (2011).
3. Sandiford, M., McLaren, S. & Neumann, N. Long-term thermal consequences of the redistribution of heat-producing elements associated with large-scale granitic complexes. *J. Metamorph. Geol.* **20**, 87–98 (2002).
4. Vielzeuf, D., Clemens, J., Pin, C. & Moinet, E. in *Granulites and Crustal Evolution* (eds Vielzeuf, D. & Vidal, Ph.) 59–85 (Springer, 1990).
5. Harley, S. The origins of granulites: a metamorphic perspective. *Geol. Mag.* **126**, 215–247 (1989).
6. Brown, M. Retrograde processes in migmatites and granulites revisited. *J. Metamorph. Geol.* **20**, 25–40 (2002).
7. Harley, S. L. A matter of time: the importance of the duration of UHT metamorphism. *J. Mineral. Petrol. Sci.* **111**, 50–72 (2016).
8. Sandiford, M. & Powell, R. Deep crustal metamorphism during continental extension: modern and ancient examples. *Earth. Planet. Sci. Lett.* **79**, 151–158 (1986).
9. Bohlen, S. On the formation of granulites. *J. Metamorph. Geol.* **9**, 223–229 (1991).
10. Kelsey, D. E. & Hand, M. On ultrahigh temperature crustal metamorphism: phase equilibria, trace element thermometry, bulk composition, heat sources, timescales and tectonic settings. *Geosci. Front.* **6**, 311–356 (2015).
11. Berglund, H. T. et al. Distributed deformation across the Rio Grande Rift, Great Plains, and Colorado Plateau. *Geology* **40**, 23–26 (2012).
12. Baldridge, W. et al. in *Developments in Geotectonics* Vol. 25 (ed. Olsen, K. H.) Ch. 6 (Elsevier, 2006).
13. Blackwell, D. et al. Temperature-at-depth maps for the conterminous US and geothermal resource estimates. *GRC Trans.* **35**, 1545–1550 (2011).
14. Schutt, D. L., Lowry, A. R. & Buehler, J. S. Moho temperature and mobility of lower crust in the western United States. *Geology* **46**, 219–222 (2018).
15. Gao, W. et al. Upper mantle convection beneath the central Rio Grande Rift imaged by P and S wave tomography. *J. Geophys. Res. Solid Earth* **109**, B3 (2004).
16. Cather, S., Chamberlin, R., Chapin, C., McIntosh, W. & Keller, G. in *GSA Special Papers* Vol. 291 (eds Keller, G. R. & Cather, S. M.) 5–25 (GSA, 1994).
17. Thompson, L. E., Velasco, A. A., Zamora, A. & Hussein, M. Geophysical constraints on the crustal structure of the Southern Rio Grande Rift. *Bull. Seismol. Soc. Am.* **107**, 1118–1128 (2017).
18. Byerly, B. L. & Lassiter, J. C. Evidence from mantle xenoliths for lithosphere removal beneath the central Rio Grande Rift. *Earth. Planet. Sci. Lett.* **355**, 82–93 (2012).
19. van Wijk, J. et al. Tectonic subsidence, geoid analysis, and the Miocene–Pliocene unconformity in the Rio Grande Rift, southwestern United States: implications for mantle upwelling as a driving force for rift opening. *Geosphere* **14**, 684–709 (2018).
20. Feucht, D., Bedrosian, P. & Sheehan, A. Lithospheric signature of late Cenozoic extension in electrical resistivity structure of the Rio Grande Rift, New Mexico, USA. *J. Geophys. Res. Solid Earth* **124**, 2331–2351 (2019).
21. Padovani, E. R. & Carter, J. L. in *The Earth's Crust* Vol. 20 (eds Heacock, J. G. et al.) 19–56 (AGU, 1977).
22. Anthony, E. Y. & Poths, J. ^{3}He surface exposure dating and its implications for magma evolution in the Potrillo volcanic field, Rio Grande Rift, New Mexico, USA. *Geochim. Cosmochim. Acta* **56**, 4105–4108 (1992).
23. Hamblock, J. et al. A composite geologic and seismic profile beneath the southern Rio Grande Rift, New Mexico, based on xenolith mineralogy, temperature, and pressure. *Tectonophysics* **442**, 14–48 (2007).
24. Bussod, G. Y. & Williams, D. R. Thermal and kinematic model of the southern Rio Grande Rift: inferences from crustal and mantle xenoliths from Kilbourne Hole, New Mexico. *Tectonophysics* **197**, 373–389 (1991).
25. Reid, M. R., Hart, S. R., Padovani, E. R. & Wandless, G. A. Contribution of metapelitic sediments to the composition, heat production, and seismic velocity of the lower crust of southern New Mexico, USA. *Earth. Planet. Sci. Lett.* **95**, 367–381 (1989).
26. Scherer, E. E. et al. Lu–Hf geochronology applied to dating Cenozoic events affecting lower crustal xenoliths from Kilbourne Hole, New Mexico. *Chem. Geol.* **142**, 63–78 (1997).
27. Reid, M. in *Granulites and Crustal Evolution* (eds Vielzeuf, D. & Vidal, Ph.) 507–522 (Springer, 1990).
28. Thomas, J. B. et al. TitaniQ under pressure: the effect of pressure and temperature on the solubility of Ti in quartz. *Contrib. Mineral. Petrol.* **160**, 743–759 (2010).
29. Tomkins, H., Powell, R. & Ellis, D. The pressure dependence of the zirconium-in-rutile thermometer. *J. Metamorph. Geol.* **25**, 703–713 (2007).
30. Holland, T. & Powell, R. An improved and extended internally consistent thermodynamic dataset for phases of petrological interest, involving a new equation of state for solids. *J. Metamorph. Geol* **29**, 333–383 (2011).
31. Brey, G. & Köhler, T. Geothermobarometry in four-phase lherzolites II. New thermobarometers, and practical assessment of existing thermobarometers. *J. Petrol.* **31**, 1353–1378 (1990).
32. Ferry, J. & Watson, E. New thermodynamic models and revised calibrations for the Ti-in-zircon and Zr-in-rutile thermometers. *Contrib. Mineral. Petrol.* **154**, 429–437 (2007).
33. Smye, A. J., Marsh, J., Vermeesch, P., Garber, J. & Stockli, D. Applications and limitations of U–Pb thermochronology to middle and lower crustal thermal histories. *Chem. Geol.* **494**, 1–18 (2018).
34. Caddick, M. J., Konopásek, J. & Thompson, A. B. Preservation of garnet growth zoning and the duration of prograde metamorphism. *J. Petrol.* **51**, 2327–2347 (2010).
35. Kroll, H., Evangelakakis, C. & Voll, G. Two-feldspar geothermometry: a review and revision for slowly cooled rocks. *Contrib. Mineral. Petrol.* **114**, 510–518 (1993).
36. Perkins, D. & Anthony, E. Y. The evolution of spinel lherzolite xenoliths and the nature of the mantle at Kilbourne Hole, New Mexico. *Contrib. Mineral. Petrol.* **162**, 1139–1157 (2011).
37. Mayhew, M. Application of satellite magnetic anomaly data to Curie isotherm mapping. *J. Geophys. Res. Solid Earth* **87**, 4846–4854 (1982).
38. Zandt, G., Myers, S. C. & Wallace, T. C. Crust and mantle structure across the Basin and Range–Colorado Plateau boundary at 37° N latitude and implications for Cenozoic extensional mechanism. *J. Geophys. Res. Solid Earth* **100**, 10529–10548 (1995).
39. Hayob, J., Essene, E. J., Ruiz, J., Ortega-Gutiérrez, F. & Aranda-Gómez, J. Young high-temperature granulites from the base of the crust in central Mexico. *Nature* **342**, 265–268 (1989).
40. Rudnick, R. L. & Cameron, K. L. Age diversity of the deep crust in northern Mexico. *Geology* **19**, 1197–1200 (1991).
41. Harley, S. L. Paragenetic and mineral–chemical relationships in orthoamphibole-bearing gneisses from Enderby Land, east Antarctica: a record of Proterozoic uplift. *J. Metamorph. Geol.* **3**, 179–200 (1985).
42. Hyndman, R. Lower-crustal flow and detachment in the North American Cordillera: a consequence of Cordillera-wide high temperatures. *Geophys. J. Int.* **209**, 1779–1799 (2017).
43. Wilson, D. et al. Lithospheric structure of the Rio Grande Rift. *Nature* **433**, 851–855 (2005).

44. Bahadori, A., Holt, W. E. & Rasbury, E. T. Reconstruction modeling of crustal thickness and paleotopography of western North America since 36 Ma. *Geosphere* **14**, 1207–1231 (2018).
45. England, P. & Houseman, G. Extension during continental convergence, with application to the Tibetan Plateau. *J. Geophys. Res. Solid Earth* **94**, 17561–17579 (1989).
46. Vissers, R., Platt, J. & Van der Wal, D. Late orogenic extension of the Betic Cordillera and the Alboran Domain: a lithospheric view. *Tectonics* **14**, 786–803 (1995).
47. Ménard, G. & Molnar, P. Collapse of a Hercynian Tibetan plateau into a late Palaeozoic European Basin and Range province. *Nature* **334**, 235–237 (1988).
48. Pattison, D. R., Chacko, T., Farquhar, J. & McFARLANE, C. R. Temperatures of granulite-facies metamorphism: constraints from experimental phase equilibria and thermobarometry corrected for retrograde exchange. *J. Petrol.* **44**, 867–900 (2003).
49. Harley, S. Refining the P–T records of UHT crustal metamorphism. *J. Metamorp. Geol.* **26**, 125–154 (2008).
50. Hansen, S. M., Dueker, K. G., Stachnik, J. C., Aster, R. C. & Karlstrom, K. E. A rootless Rockies—support and lithospheric structure of the Colorado Rocky Mountains inferred from CREST and TA seismic data. *Geochem. Geophys. Geosyst.* **14**, 2670–2695 (2013).
51. Prol-Ledesma, R.-M., Carrillo-de la Cruz, J.-L., Torres-Vera, M.-A., Membrillo-Abad, A.-S. & Espinoza-Ojeda, O.-M. Heat flow map and geothermal resources in Mexico. *Terra Digitalis* **2**, https://doi.org/10.22201/igg.25940694.2018.2.51 (2018).
52. Hansen, S. M., Dueker, K. & Schmandt, B. Thermal classification of lithospheric discontinuities beneath USArray. *Earth. Planet. Sci. Lett.* **431**, 36–47 (2015).
53. McKenzie, D. & Bickle, M. The volume and composition of melt generated by extension of the lithosphere. *J. Petrol.* **29**, 625–679 (1988).
54. Winter, J. D. *Principles of Igneous and Metamorphic Petrology* (Pearson, 2013).
55. Lachenbruch, A. H. & Sass, J. in *The Earth's Crust* Vol. 20 (eds Heacock, J. G. et al.) 626–675 (AGU, 1977).

Methods

Sample descriptions. All samples analysed and described in this study are from KBH, New Mexico (31° 57′ 40.4″ N, 106° 57′ 57.0″ W).

Mafic granulites. We studied two mafic granulites with similar mineralogies and textures.

Sample 18KH40 is a coarse-grained, equigranular orthogneiss (200–2,000 µm grain diameter) composed of plagioclase (~80 vol.%) + orthopyroxene (15 vol.%) + clinopyroxene (<5 vol.%) with accessory apatite, zircon and an unidentified oxide phase. Plagioclase grains constitute the majority of the sample matrix and have embayed grain boundaries, indicative of crystallization from a melt phase. Orthopyroxene and clinopyroxene are present as porphyroblasts (500–1,000 µm diameter) and exhibit straight grain boundaries with matrix plagioclase, indicative of textural equilibrium. Pyroxenes are also observed as intergrowths, forming aggregates 2–3 mm in diameter. Orthopyroxene blasts host abundant, rounded zircon inclusions (100–200 µm diameter). Finally, lobate clots of mafic glass are interpreted to represent basaltic melt pockets derived from the host alkali basalt responsible for entrainment.

Sample 18KH43 is a coarse-grained, equigranular orthogneiss (200–2,000 µm grain diameter) composed of plagioclase (80 vol.%) + orthopyroxene (15 vol.%) + clinopyroxene (5 vol.%) with accessory apatite, zircon and an unidentified oxide phase. Textures and phase relationships in 18KH43 are similar to sample 18KH40, with the exception that zircon is hosted within matrix grains of plagioclase and orthopyroxene blasts.

Felsic granulites. We also studied seven garnet paragneiss xenoliths with the following assemblage: ternary feldspar ± plagioclase + quartz + prismatic sillimanite + garnet + ilmenite + rutile + zircon. All samples exhibit garnet porphyroblasts within a matrix of feldspars, quartz and sillimanite, in addition to accessory rutile, ilmenite and zircon. Matrix grains commonly exhibit irregular, lobate grain boundaries, indicative of the presence or former presence of a melt phase. Rutile has lamellae and/or rims of ilmenite but is euhedral, indicating textural equilibrium with the matrix. There is often a pervasive melt phase along grain boundaries and associated with quartz-feldspar leucosomes. Differences in grain size, mineral modes, intensity of deformation (foliation), feldspar textural relationships, garnet inclusion assemblages and the degree of kelyphitization of garnet are the main distinguishing features between the studied samples and are described in the following for each xenolith.

Sample DEKH2 is a lineated, fine-grained garnet paragneiss (100–500 µm grain diameter) composed of ternary feldspar (~25 vol.%) + quartz (40 vol.%) + prismatic sillimanite (20 vol.%) + garnet (15 vol.%) with accessory ilmenite, rutile and zircon. Porphyroblasts of garnet (0.2–3 mm grain diameter) are elongate in the lineation direction and contain rounded quartz and zircon inclusions (50–100 µm diameter); kelyphitic breakdown textures penetrate the outermost 100–200 µm of garnet crystal rims.

Sample JC18KH9 is a weakly foliated, fine-grained garnet paragneiss (100–400 µm grain diameter) composed of ternary feldspar (~25 vol.%) + plagioclase (15 vol.%) + quartz (20 vol.%) + prismatic sillimanite (10 vol.%) + garnet (30 vol.%) with accessory ilmenite, rutile and zircon. Porphyroblasts of garnet (0.2–6 mm grain diameter) contain rounded quartz inclusions (50–300 µm diameter) and kelyphitic breakdown textures that are pervasive, in some cases consuming the entire grain (up to ~1 mm). Some plagioclase is present as patchy mesoperthite lamellae (~20 µm) within ternary feldspar.

Sample JC18KH15 is a weakly foliated, fine-grained garnet paragneiss (100–400 µm grain diameter) composed of ternary feldspar (~35 vol.%) + plagioclase (5 vol.%) + quartz (30 vol.%) + prismatic sillimanite (15 vol.%) + garnet (15 vol.%) with accessory ilmenite, rutile and zircon. Garnet porphyroblasts (0.2–3 mm diameter) are generally inclusion free, but some contain rounded quartz and zircon inclusions (50–200 µm diameter) and have kelyphitic breakdown textures that consume the outermost 100–500 µm of grains. Some of the largest garnet porphyroblasts have inclusion-rich cores and inclusion-free rims.

Sample JC18KH16 is a foliated, coarse-grained garnet paragneiss (200–1,000 µm grain diameter) composed of ternary feldspar (~30 vol.%) + plagioclase (10 vol.%) + quartz (30 vol.%) + prismatic sillimanite (10 vol.%) + garnet (20 vol.%) with accessory ilmenite, rutile and zircon. Garnet porphyroblasts (0.1–2 mm diameter) are elongate in the foliation direction, occasionally contain rounded quartz and zircon inclusions (50–200 µm) and have kelyphitic breakdown textures that span the outermost 100–300 µm of crystal rims.

Sample JC18KH28 is a weakly foliated, fine-grained garnet paragneiss (100–500 µm grain diameter) composed of ternary feldspar (~40 vol.%) + plagioclase (10 vol.%) + quartz (20 vol.%) + prismatic sillimanite (15 vol.%) + garnet (15 vol.%) with accessory ilmenite, rutile and zircon. Garnet porphyroblasts (0.1–3 mm diameter) are rarely elongate in the foliation direction, frequently contain rounded inclusions of quartz, zircon, and rutile (50–200 µm diameter) and exhibit minimal kelyphitic breakdown textures over the outermost ~100 µm of crystal rims. Plagioclase occasionally occurs as a matrix phase, but generally is present as patchy lamellae ~20 µm thick within ternary feldspars.

Sample JC18KH31 is a weakly foliated, fine-grained garnet paragneiss (50–300 µm grain diameter) composed of ternary feldspar (~40 vol.%) + plagioclase (10 vol.%) + quartz (25 vol.%) + prismatic sillimanite (5 vol.%) + garnet (10 vol.%) with accessory ilmenite, rutile and zircon. Garnet porphryoblasts (0.1–3.5 mm diameter) contain rounded inclusions of quartz and zircon (50–200 µm) and have extensive kelyphitic rims that, in some cases, are ~1 mm thick. Plagioclase occurs as both a matrix phase and as mesoperthite lamellae, ~30 µm thick within ternary feldspar grains.

Sample JC18KH32 is a weakly foliated, fine-grained garnet paragneiss (100–400 µm grain diameter) composed of ternary feldspar (~35 vol.%) + plagioclase (5 vol.%) + quartz (30 vol.%) + prismatic sillimanite (10 vol.%) + garnet (20 vol.%) with accessory ilmenite, rutile and zircon. Garnet porphyroblasts (0.1–4 mm diameter) contain inclusions of quartz, zircon and rutile and have minimal kelyphitic breakdown textures over the outermost 100–200 µm of crystal rims. Plagioclase occurs as a rare matrix phase but is present primarily as ~20-µm-thick lamellae within ternary feldspar grains.

Electron microprobe analysis. Major element mineral concentrations were measured using the Cameca SX-5 electron microprobe (EPMA) in the Materials Characterization Lab at the Pennsylvania State University. Natural and synthetic mineral samples were used as standards. Analytical conditions comprised a beam current of 30 nA, an accelerating voltage of 20 kV and a focused beam (<1 µm spot size). Peak and background counting times for the measured elements ranged from 20 s to 30 s each.

Concentrations of Ti in quartz and Zr in rutile, respectively, were measured on the Cameca SX-100 at the Rensselaer Polytechnic Institute Earth and Environmental Sciences Laboratory. The Ti and Zr were measured simultaneously on four large pentaerythritol (LPET) crystals while the silicon (Si) and Ti matrices for quartz and rutile were measured on a thallium acid pthalate (TAP) crystal. Run conditions comprised a beam current of 200 nA, an accelerating voltage of 15 kV and a focused beam (<1 µm spot size). Peak and background counting times were 180 s and 60 s for quartz and rutile, respectively. In quartz, beam damage was minimal; changes in measured Ti and Si within the time span of a single spot did not vary outside of analytical uncertainty.

Intragrain Zr-in-rutile variation was almost ubiquitously smaller than measurement uncertainty, but intergrain Zr-in-rutile concentrations were not homogeneous; rutile grains adjacent to one another exhibited variations in [Zr] >1,000 ppm (Extended Data Fig. 9). To ensure selection of equilibrium Zr concentrations for 4+ thermometry, average [Zr] for each sample was chosen on the basis of measured concentrations from rutile closest to zircon (<1 mm distance for all samples) that were reproducible in several grains. Care was taken to avoid secondary fluorescence of Zr, and no rutiles were measured closer than ~200 µm to a zircon.

Laser-ablation split-stream ICP-MS. Heavy mineral separates were obtained from four samples (JC18KH9, JC18KH16, JC18KH28, JC18KH32) using standard mineral separation techniques. Zircon was picked from the 0–200 and 200–400 µm size fractions, and grains were mounted in epoxy such that unpolished facets were exposed to the surface. Mounts were washed in DI water and ethanol prior to analysis.

All laser-ablation analyses on zircon and rutile were carried out at the University of California, Santa Barbara laser-ablation split-stream mass spectrometry (LASS) laboratory, in which U–Pb isotopes and trace element are measured on the same analytical spot. The method has been described in detail elsewhere[56]. The laboratory set-up for these sessions consisted of a Photon Machines 193 nm excimer with HelEx cell coupled to two mass spectrometers: a Nu Instruments Plasma 3D multicollector inductively coupled plasma mass spectrometer (ICP-MS) (U–Th–Pb isotopes) and an Agilent 7700 S quadrupole ICP-MS (trace elements).

Zircon depth profiling analyses were carried out with a 50 µm laser spot size, a laser frequency of 2 Hz, a 150 s ablation time and an ablation rate of ~50 nm pulse^{-1}. Final pit depths were measured on a Zygo Optical Profilometer at Penn State University and were consistently ~15 µm for all zircon samples. Rutile LASS spot analyses were carried out with a 35 µm laser spot size, a laser frequency of 4 Hz and a 15 s ablation time.

All LASS data were processed using Iolite version 3.0[56]; downhole and machine drift are corrected in Iolite from measurements of matrix-matched U–Pb and trace-element standards that are interspersed within analyses of unknowns. Primary zircon standards were 91500 zircon[57] and GJ-1 zircon[58] for U–Pb and trace elements, respectively. GJ-1 and Plešovice zircon[59] were used as secondary reference materials to determine uncertainties for U–Pb measurements. Measured secondary standard ages were within <2% of their accepted ages (Supplementary Table 4). For rutile, Kragerø rutile[60] was analysed as a primary U–Pb standard, and BHVO-2 glass was used as a primary trace-element standard. Measured Kragerø rutile [Zr] was 1,178 ± 123 ppm (n = 22; 2σ), within the expected range of [Zr] content for Kragerø (1,100–1,200 ppm).

Following processing in Iolite, U–Pb data were analysed in IsoplotR[61]. Discrete zircon zones were chosen on the basis of ^{207}Pb/^{206}Pb-corrected ^{238}U/^{206}Pb age and trace-element plateaus consisting of ≥8 laser shots (that is, 400 nm zircon thickness). Age zones are typically defined by an isochron whose endmembers

are a lower-age intercept and modern common Pb ($^{207}Pb/^{206}Pb = 0.835 \pm 0.010$) (ref. [62]). For each defined zone, an average of all selected shots was taken for trace elements including Ti.

Thermobarometry and phase equilibria modelling. Estimates of *P* and *T* were derived for seven metapelites from the intersection of the garnet–aluminium–silicate–plagioclase (GASP), Ti-in-quartz and Zr-in-rutile equilibria. For GASP, endmember mineral activities were calculated from EPMA measurements using AX62 software[8], and equilibrium *PT* coordinates were calculated in Thermocalc[63] (calcmode 3 using the thermodynamic database of Holland and Powell[30]). Ti-in-quartz and Zr-in-rutile equilibria were calculated using expressions from Thomas et al.[28] and Tomkins et al.[29], respectively. Average *PT* intersections for all chosen equilibria were calculated using a Monte Carlo scheme in which the intersection between each of the three equilibria was calculated 10,000 times. Each iteration randomly drew values of mineral composition from Gaussian distributions that reflect analytical uncertainties. Computed *PT* values, uncertainties and covariance are displayed as error ellipses on Fig. 4a.

PT pseudosections were constructed for four KBH spinel lherzolite xenoliths whose bulk compositions have been previously published (KLB-1[64], KH-11 and KH-29[36]) and two metapelite xenoliths (JC18KH9, JC18KH28) using Thermocalc[63] and the thermodynamic database of Holland and Powell[30]. For lherzolites, phase relations were computed in the system NCFMASCrO[65] between 800 and 1,600 °C and between 0 and 3 GPa using the *a–X* relations of ref. [65]. For metapelites, phase relations were computed in the system MnNCKFMASHTO between 600 and 1,100 °C and between 0.5 and 1.5 GPa using the *a–X* relations of ref. [66]. Bulk rock compositions for lherzolites and metapelites in mol.% are provided in Supplementary Table 5; bulk rock compositions for metapelites were measured at Franklin and Marshall College by X-ray fluorescence of fused glass discs. The topology of each pseudosection is sensitive to bulk rock Fe_2O_3 content. We used a nominal concentration of 0.1 mol.% Fe_2O_3 for each lherzolite section; an increase in Fe_2O_3 will increase the maximum pressure at which spinel is predicted to be stable and therefore maximum estimated *P* for KBH lherzolite xenoliths. For example, doubling of Fe_2O_3 (to 0.2 mol.%) results in approximately a 0.1 GPa increase in the maximum *P* for the spinel stability field[65]. Pyroxene compositions used for two-pyroxene thermometry are from ref. [64] for KLB-1 and ref. [36] for KH-11 and KH-29.

Thermal modelling. To investigate potential heating mechanisms, we computed the thermal field in a lithospheric column under two tectonic configurations: (1) depth-dependent pure shear and (2) thermal equilibration following removal of lithospheric mantle. We solved the heat equation:

$$\frac{\partial T}{\partial t} = \alpha \frac{\partial^2 T}{\partial t^2} - u \frac{\partial T}{\partial z} + A_{\mathrm{rad}}$$

where *T* is temperature, *t* is time, α is thermal diffusivity, *z* is depth, *u* is velocity due to extension and A_{rad} is crustal heat production. The solution *T(z,t)* was tracked using a one-dimensional implicit finite difference scheme for heat conduction and upwind differences for advection. Dirichlet boundary conditions were imposed at the surface ($T = 20$ °C at $z = 0$ km) and base ($T = 1{,}450$ °C at $z = 125$ km) of the computation domain. Material properties were as follows: $\alpha_{\mathrm{crust}} = 8 \times 10^{-7}$ m^2 s^{-1}; $\rho_{\mathrm{crust}} = 2.8$ g cc^{-1}; $C_p^{\mathrm{crust}} = 800$ J kg^{-1} °C^{-1}; $\alpha_{\mathrm{mantle}} = 10^{-6}$ m^2 s^{-1}; $\rho_{\mathrm{mantle}} = 3.3$ g cc^{-1}; $C_p^{\mathrm{crust}} = 1{,}250$ J kg^{-1} °C^{-1}, where ρ is density and C_p is specific heat. Crustal heat production is assumed to follow an exponential distribution, $A(z) = A_0 e^{-z/z_h}$ with surface heat production, A_0, of 3 μW m^{-3} and an e-folding depth, z_h, of 8 km; heat production is assumed to be negligible in the mantle. At the start of each calculation, the Moho was set at 40 km, and the lithosphere–asthenosphere boundary is assumed to coincide with the 1,330 °C isotherm. The energetics of fusion within the mantle were incorporated through the expressions presented by McKenzie and Bickle[53]; crustal melting was not incorporated into the calculations.

For case (1), we followed the kinematic framework presented by Bown and White[67] and divided the lithosphere into two layers, corresponding to the crust and lithospheric mantle, each of which were prescribed to thin independently from one another by factors of β and δ, respectively. For case (2), asthenopheric temperatures were imposed at depths beneath 40 km, simulating instantaneous removal of lithospheric mantle; *T* beneath 40 km was held constant throughout the calculation duration. Each of the calculations was performed for 35 Myr with an initial, steady-state geotherm computed with the material properties and heat production distribution presented in the preceding.

Data availability

Zircon and rutile U–Pb and trace-element data, whole-rock X-ray fluorescence data and mineral electron microprobe analyses are available in this published article and its Supplementary Information files, as well as at https://doi.org/10.17605/OSF.IO/S7MF6. Source data are provided with this paper.

Code availability

The MATLAB code used for the thermal modelling is available from the corresponding authors upon request.

References

56. Paton, C., Hellstrom, J., Paul, B., Woodhead, J. & Hergt, J. Iolite: freeware for the visualisation and processing of mass spectrometric data. *J. Anal. At. Spectrom.* **26**, 2508–2518 (2011).
57. Wiedenbeck, M. et al. Further characterisation of the 91500 zircon crystal. *Geostand. Geoanal. Res.* **28**, 9–39 (2004).
58. Jackson, S. E., Pearson, N. J., Griffin, W. L. & Belousova, E. A. The application of laser ablation–inductively coupled plasma–mass spectrometry to in situ U–Pb zircon geochronology. *Chem. Geol.* **211**, 47–69 (2004).
59. Sláma, J. et al. Plešovice zircon—a new natural reference material for U–Pb and Hf isotopic microanalysis. *Chem. Geol.* **249**, 1–35 (2008).
60. Bracciali, L., Parrish, R. R., Horstwood, M. S., Condon, D. J. & Najman, Y. UPb LA-(MC)-ICP-MS dating of rutile: new reference materials and applications to sedimentary provenance. *Chem. Geol.* **347**, 82–101 (2013).
61. Vermeesch, P. IsoplotR: a free and open toolbox for geochronology. *Geosci. Front.* **9**, 1479–1493 (2018).
62. Stacey, J. T. & Kramers, J. Approximation of terrestrial lead isotope evolution by a two-stage model. *Earth. Planet. Sci. Lett.* **26**, 207–221 (1975).
63. Powell, R. & Holland, T. An internally consistent dataset with uncertainties and correlations: 3. Applications to geobarometry, worked examples and a computer program. *J. Metamorph. Geol.* **6**, 173–204 (1988).
64. Davis, F. A., Tangeman, J. A., Tenner, T. J. & Hirschmann, M. M. The composition of KLB-1 peridotite. *Am. Mineral.* **94**, 176–180 (2009).
65. Jennings, E. S. & Holland, T. J. A simple thermodynamic model for melting of peridotite in the system NCFMASOCr. *J. Petrol.* **56**, 869–892 (2015).
66. White, R., Powell, R., Holland, T., Johnson, T. & Green, E. New mineral activity–composition relations for thermodynamic calculations in metapelitic systems. *J. Metamorph. Geol.* **32**, 261–286 (2014).
67. Bown, J. W. & White, R. S. Effect of finite extension rate on melt generation at rifted continental margins. *J. Geophys. Res. Solid Earth* **100**, 18011–18029 (1995).
68. Wessel, P. & Smith, W. H. F. Free software helps map and display data. *Eos Trans. AGU* **72**, 441–448 (1991).
69. Benisek, A., Dachs, E. & Kroll, H. A ternary feldspar-mixing model based on calorimetric data: development and application. *Contrib. Mineral. Petrol.* **160**, 327–337 (2010).
70. Grove, T. L., Baker, M. B. & Kinzler, R. J. Coupled CaAl–NaSi diffusion in plagioclase feldspar: experiments and applications to cooling rate speedometry. *Geochim. Cosmochim. Acta* **48**, 2113–2121 (1984).
71. Cherniak, D., Watson, E. & Wark, D. Ti diffusion in quartz. *Chem. Geol.* **236**, 65–74 (2007).
72. Carlson, W. D. Rates of Fe, Mg, Mn, and Ca diffusion in garnet. *Am. Mineral.* **91**, 1–11 (2006).
73. Cherniak, D., Manchester, J. & Watson, E. Zr and Hf diffusion in rutile. *Earth. Planet. Sci. Lett.* **261**, 267–279 (2007).
74. Clark, C., Fitzsimons, I. C., Healy, D. & Harley, S. L. How does the continental crust get really hot? *Elements* **7**, 235–240 (2011).
75. Houseman, G. A., McKenzie, D. P. & Molnar, P. Convective instability of a thickened boundary layer and its relevance for the thermal evolution of continental convergent belts. *J. Geophys. Res. Solid Earth* **86**, 6115–6132 (1981).
76. Ducea, M. & Saleeby, J. A case for delamination of the deep batholithic crust beneath the Sierra Nevada, California. *Int. Geol. Rev.* **40**, 78–93 (1998).
77. Bartol, J. & Govers, R. A single cause for uplift of the Central and Eastern Anatolian plateau? *Tectonophysics* **637**, 116–136 (2014).
78. Nelson, K. Are crustal thickness variations in old mountain belts like the Appalachians a consequence of lithospheric delamination? *Geology* **20**, 498–502 (1992).
79. Seber, D., Barazangi, M., Ibenbrahim, A. & Demnati, A. Geophysical evidence for lithospheric delamination beneath the Alboran Sea and Rif–Betic mountains. *Nature* **379**, 785–790 (1996).

Acknowledgements

A.J.S. acknowledges support from the Slingerland Early Career Fellowship at Penn State and NSF grant EAR-2025122. J.M.G. acknowledges postdoctoral support from NSF Grant OISE-1545903 and Penn State. L. Jolivet, B. Hacker, R. Rudnick, L. Lavier, J. Reimink and R. Holder are thanked for comments and discussion that improved earlier versions of the manuscript. R. Rudnick and M. Ringwood are thanked for lending samples. S. Seman is thanked for assisting with fieldwork. Figure 1 was prepared using GMT 6.1[68].

Author contributions

A.J.S. conceived the study and created thermal models. J.H.C. and A.J.S. conducted sample collection. J.H.C., J.M.G. and A.R.C.K.-C. collected all data. J.H.C., A.J.S. and J.M.G. wrote the manuscript.

Competing interests

The authors declare no competing interests.

Additional information

Extended data is available for this paper at https://doi.org/10.1038/s41561-020-0640-z.

Supplementary information is available for this paper at https://doi.org/10.1038/s41561-020-0640-z.

Correspondence and requests for materials should be addressed to J.H.C. or A.J.S.

Peer review information Primary Handling Editor: Rebecca Neely.

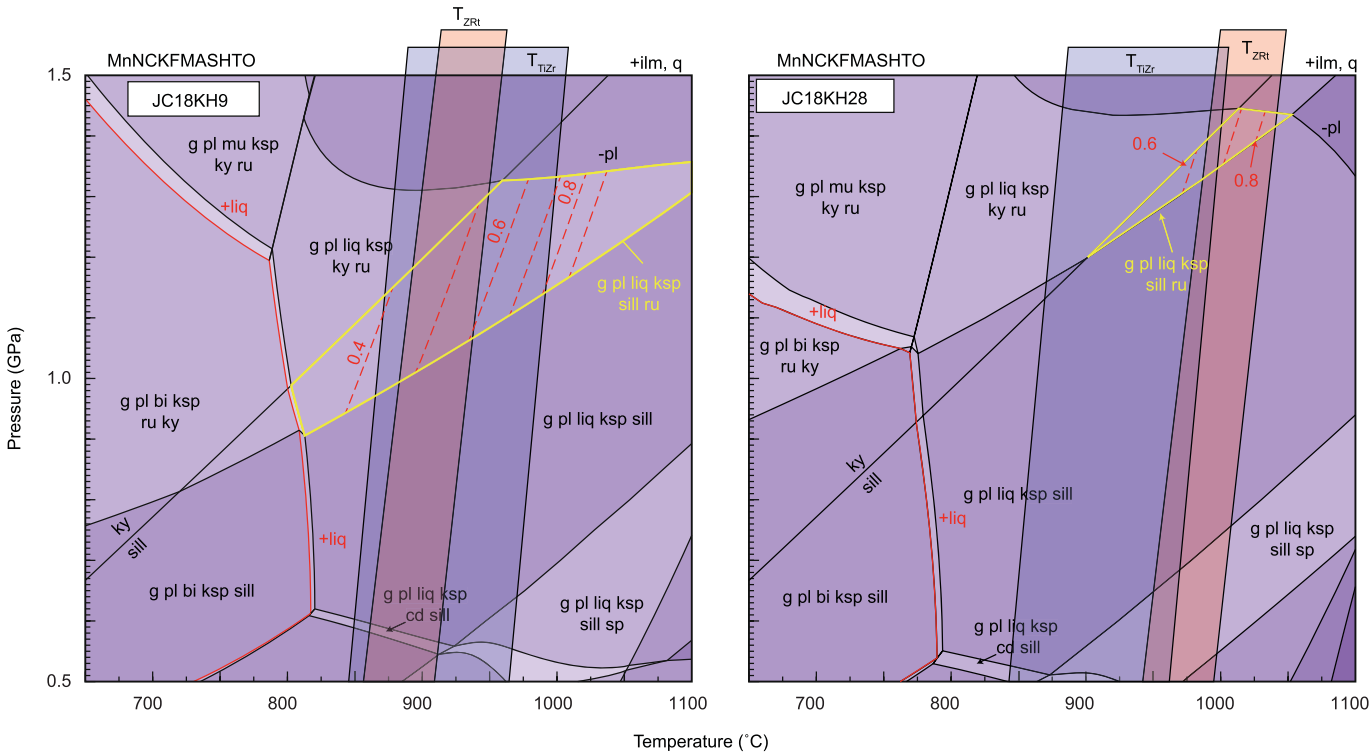

Extended Data Fig. 1 | PT pseudosections for Kilbourne Hole Metapelites JC18KH9 and JC18KH28. Yellow field shows peak assemblage; blue and red bars represent range of measured Ti-in-zircon and Zr-in-rutile T-estimates. Dashed red lines represent melt mode isopleths (in mol.%).

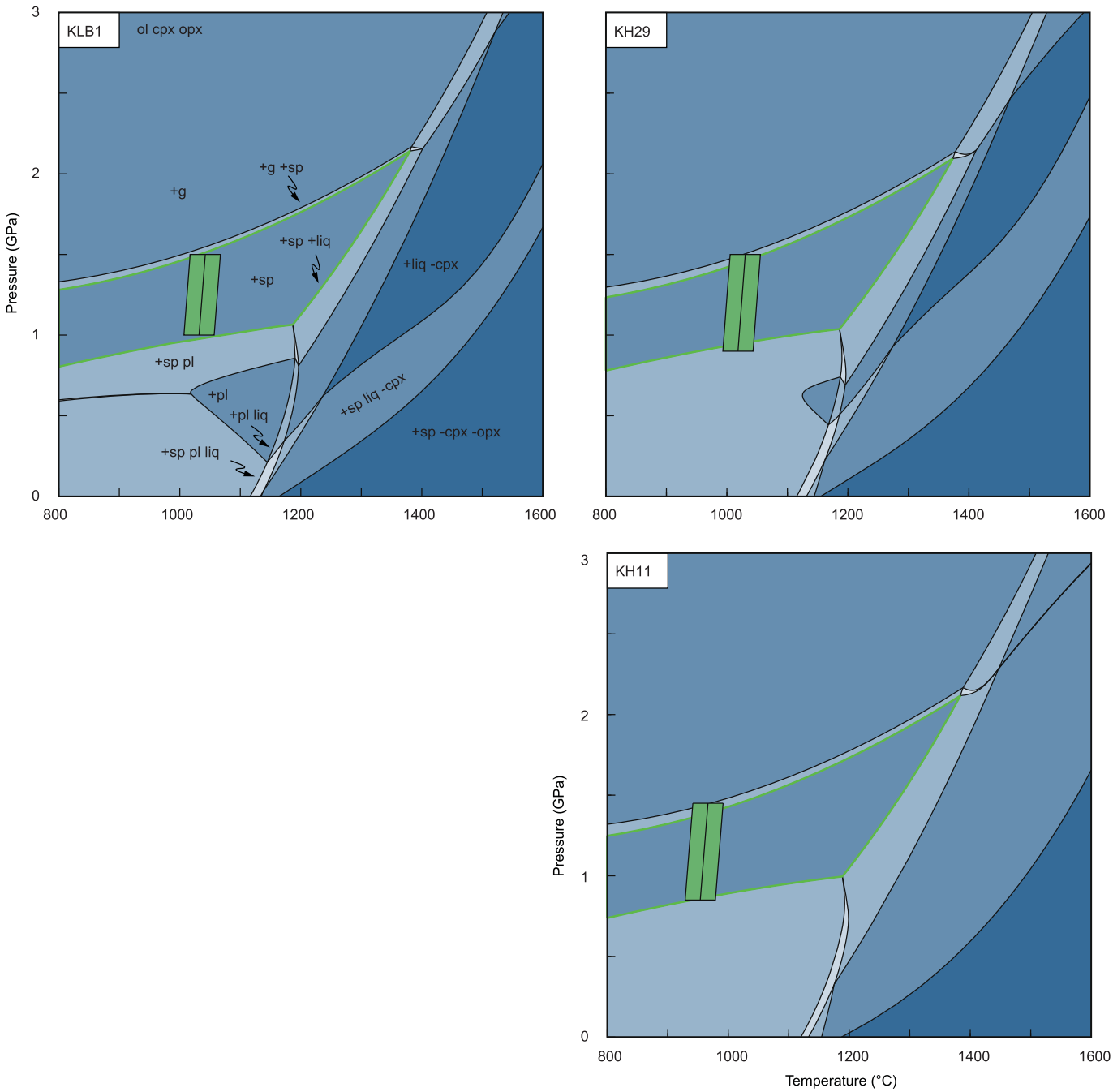

Extended Data Fig. 2 | Mantle pseudosections for Kilbourne Hole lherzolite xenoliths KH-11, KH-29, and KLB-1. The assemblage for KBH lherzolites (clinopyroxene-orthopyroxene-olivine-spinel) is outlined in green. Average temperatures Fe-Mg and Na exchange between coexisting clinopyroxene and orthopyroxenes are calculated using the calibration of Brey & Köhler (1990)[31].

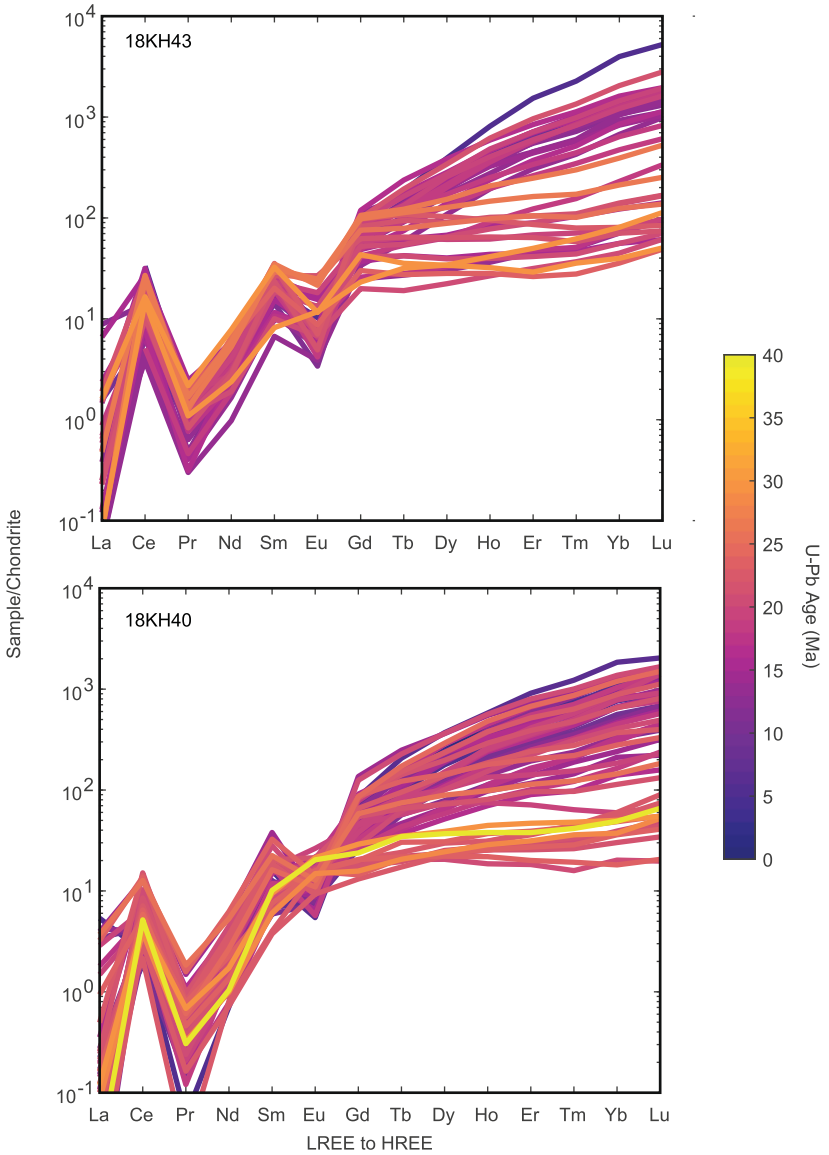

Extended Data Fig. 3 | Metaigneous xenolith zircon REE data. Each pattern represents a single zone from LASS-ICP-MS depth profiling as described in Methods. Zones with U-Pb ages dated to early in the RGR history have flat HREE patterns, suggesting that garnet was present in these rocks at this time — consistent with higher pressures from thicker overlying crust.

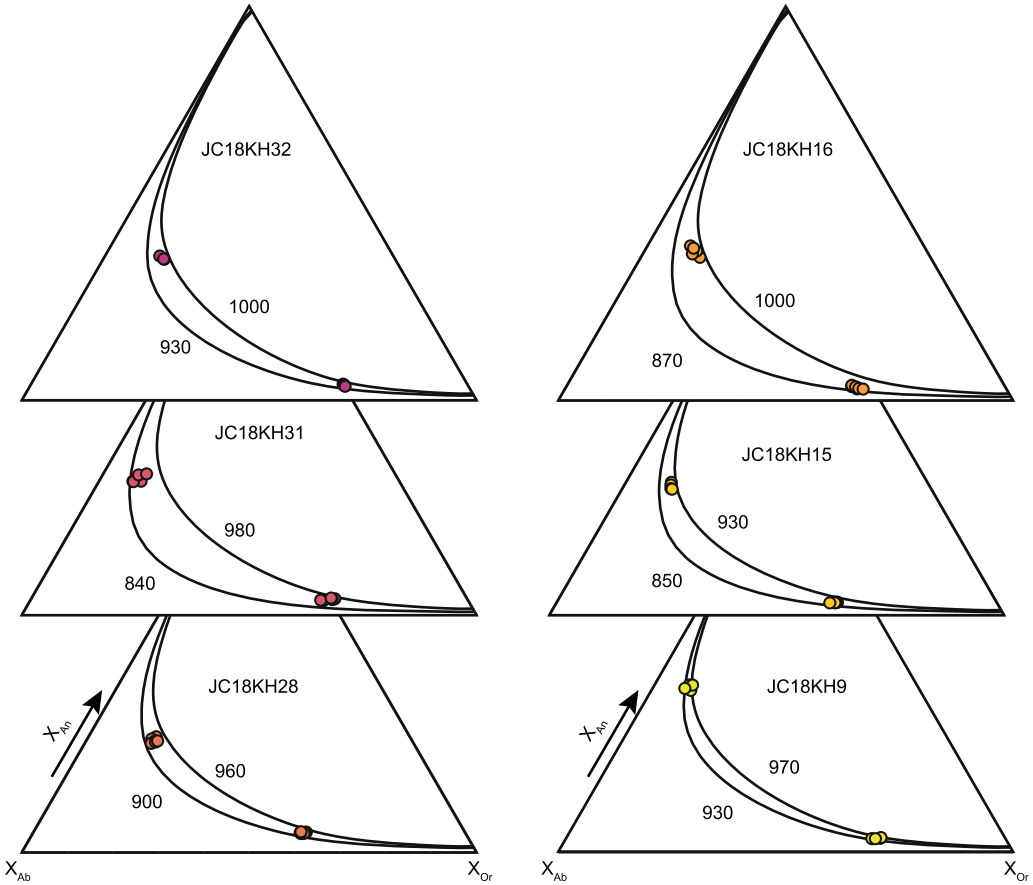

Extended Data Fig. 4 | Coexisting K-feldspar and plagioclase compositions in Kilbourne Hole metapelite xenoliths. Bounding isotherms are calculated using the feldspar mixing models of ref. [69] and are shown as black lines labeled with respective temperature.

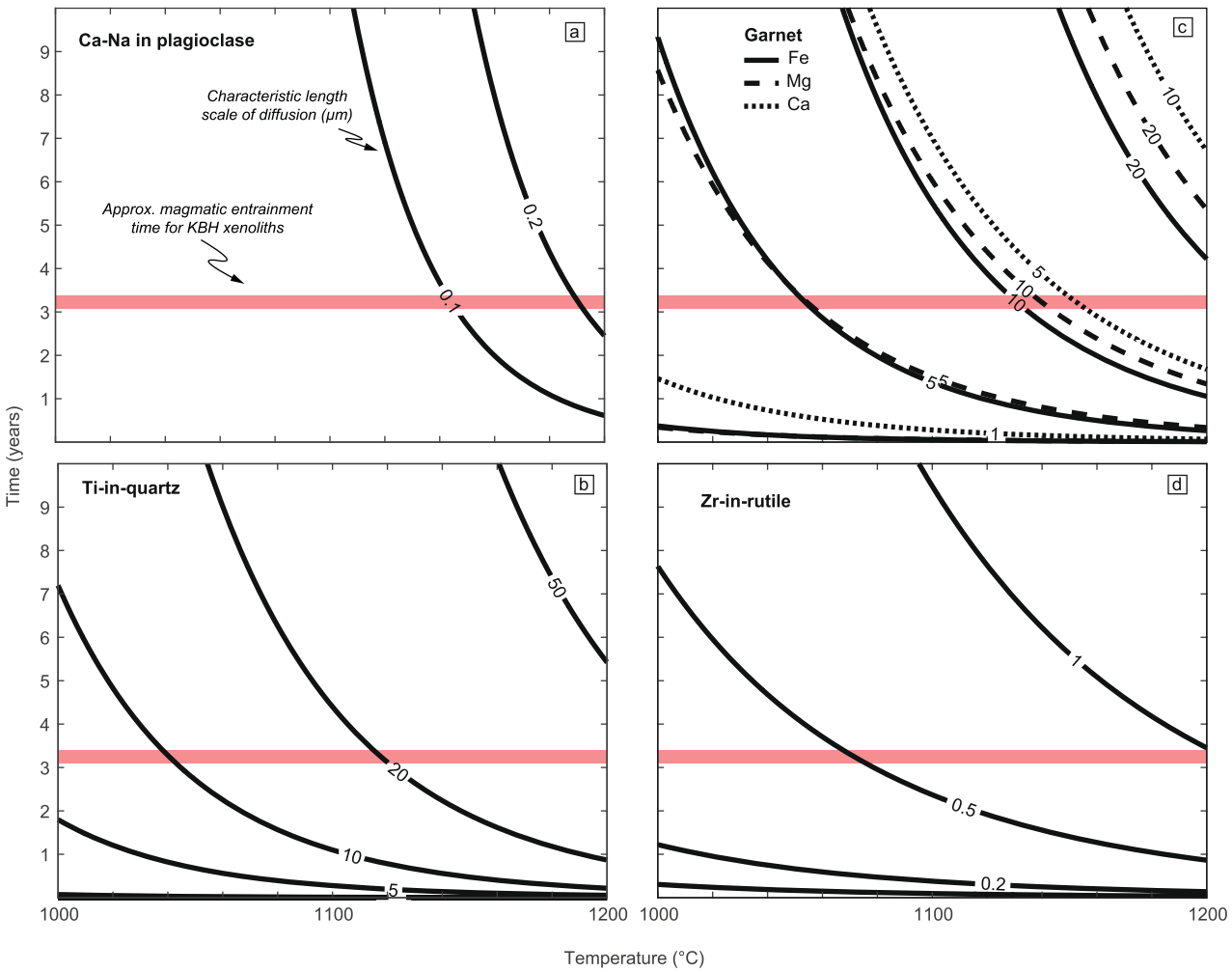

Extended Data Fig. 5 | Select major and trace element diffusion length scales for Kilbourne Hole xenolith magmatic entrainment timescales. Characteristic length scales of diffusion were calculated for key mineral chemistry used in xenolith thermobarometry: Ca-Na exchange in plagioclase[70] **a**, Ti-in-quartz[71] **b**, Garnet major elements at graphite-oxygen fO_2[72] **c**, and Zr-in-rutile[73] (**d**). Published magmatic heating timescales for KBH xenoliths have been estimated from Ca-in-olivine profiles[36] and are shown as orange highlighted areas.

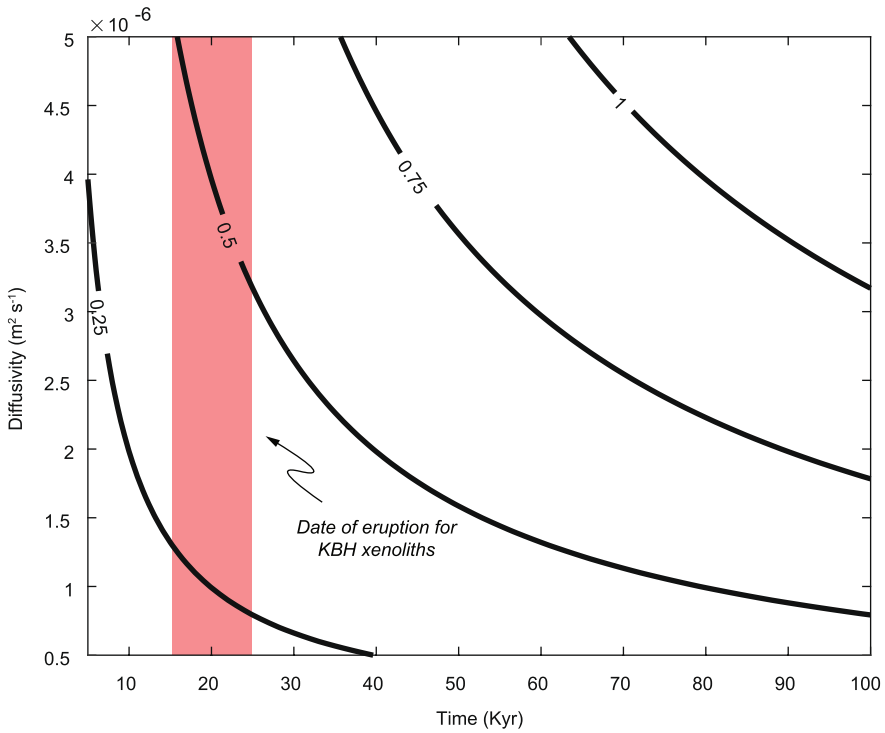

Extended Data Fig. 6 | Length scales of heat conduction in rock. Black contours show characteristic length scale of diffusion ($\sqrt{\kappa t}$) for range of times since eruption of KBH xenoliths. Date of eruption is from ref. [22].

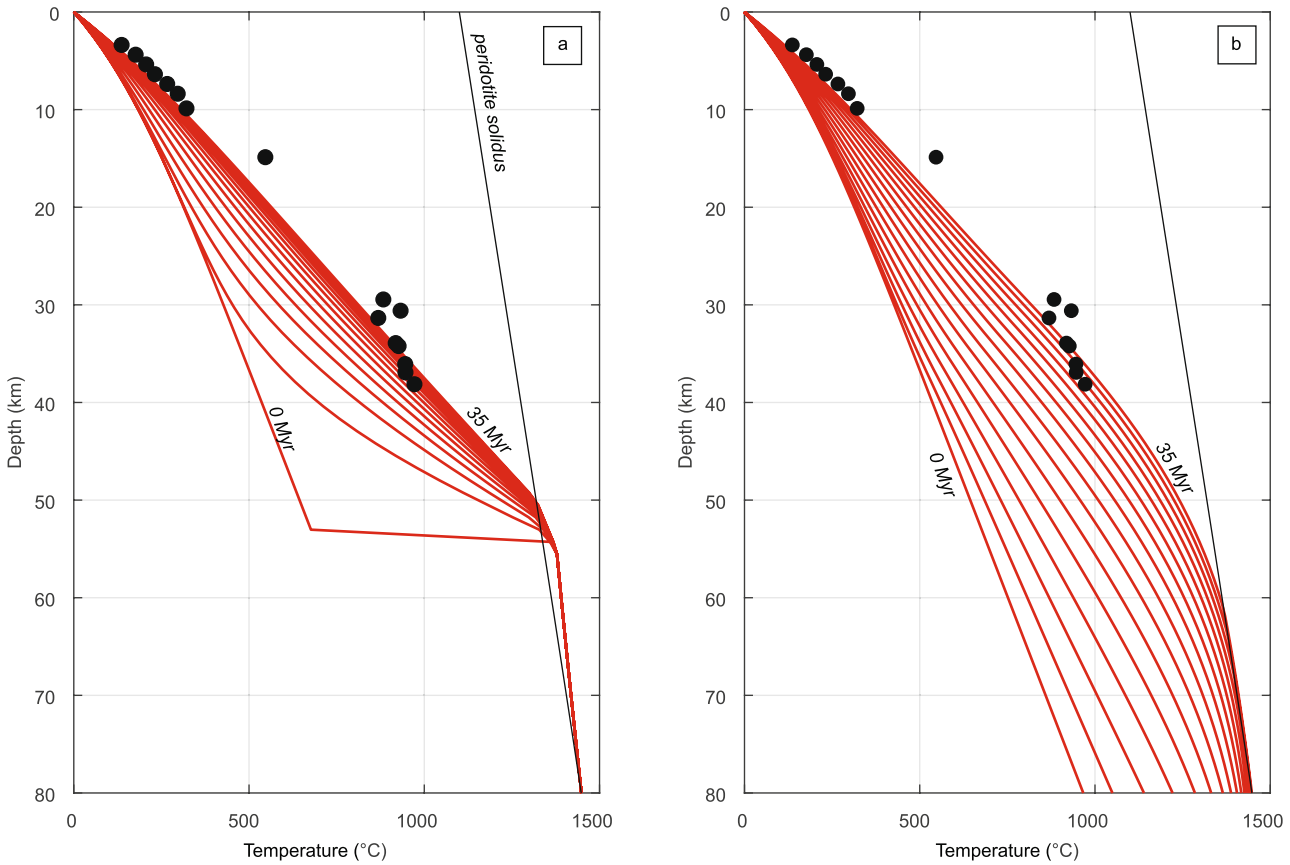

Extended Data Fig. 7 | Thermal-kinematic calculations of a lithospheric column undergoing lithospheric thinning. a, evolution of lithospheric geotherm following instantaneous juxtaposition of asthenosphere and lithosphere at 55 km, 35 Ma. Black markers represent KBH *PT* constraints discussed in main text; geotherm plotted every 1 Myr. **b**, evolution of lithospheric geotherm during depth-dependent extension in which the crust and mantle are thinned by factors of 1.25 and 6, respectively.

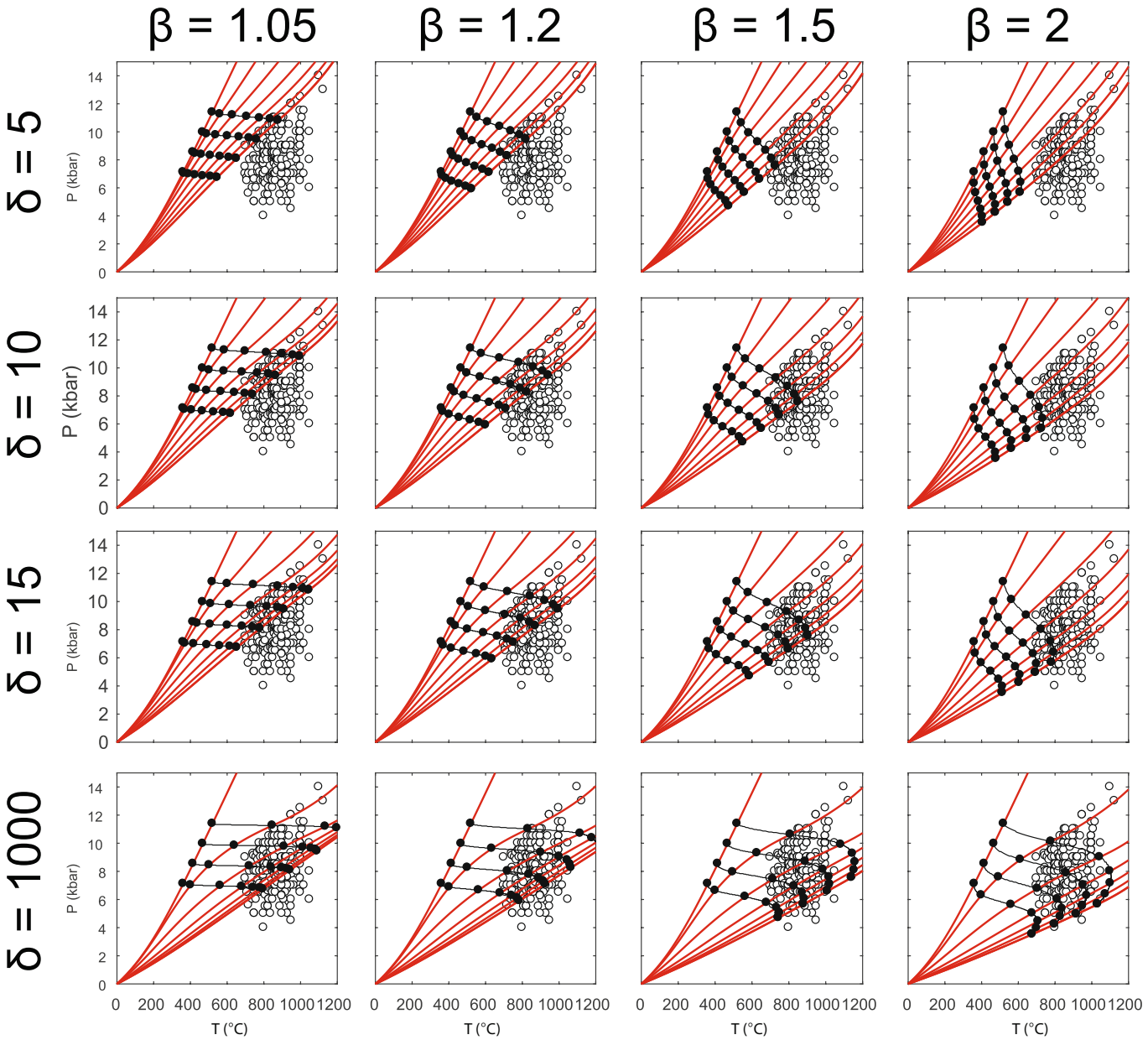

Extended Data Fig. 8 | Thermal-kinematic calculations of a lithospheric column undergoing depth-dependent extension. Each panel shows the lithospheric geotherm (red line) and PTt paths (black markers and lines) for rocks at initial depths of 25, 30, 35 and 40 km, undergoing different combinations of mantle (δ) and crustal thinning (β). The duration of each model calculation is 30 Myr and geotherms and marker nodes are plotted at 5 Myr increments. White markers are PT estimates from a global compilation of exhumed granulites[74]. All calculations assume an initial lithospheric thickness of 125 km, a crustal thickness of 40 km, a mantle potential temperature of 1330 °C, an exponential distribution of heat production throughout the crust with a surface value of 3 $\mu W.m^{-3}$ and an e-folding length of 8 km, crustal and mantle densities of 2.9 and 3.3 $kg.m^{-3}$ respectively, and crustal and mantle and thermal diffusivities of 10^{-6} and $8x10^{-7}$ $m^2.s^{-1}$, respectively. Calculations do not take into account the effects of latent heat or the temperature-dependence of thermal conductivity. These models illustrate that replacement of the lowermost lithosphere by hotter, less dense asthenospheric mantle drives conductive heating of the remaining, overlying lithosphere; the timescale of metamorphism associated with this heating is controlled by the thickness of, and rate of extension within, the overlying lithosphere. Provided that the rate of crustal thinning is less than the rate of heat conduction through the crust, peak metamorphic *T* may occur during decompression. Many exhumed granulite terranes record a high-*T* clockwise-sense *PT* segment, and the tectonic sequence represented by these models (crustal thickening, lithospheric removal, and extension) is recognized in a number of modern orogens: (1) Tibet[75], (2) Sierra Nevada[76], (3) Anatolian plateau[77], (4) south-central Appalachians[78], (5) Alboran Sea and Betic-Rif mountains[79].

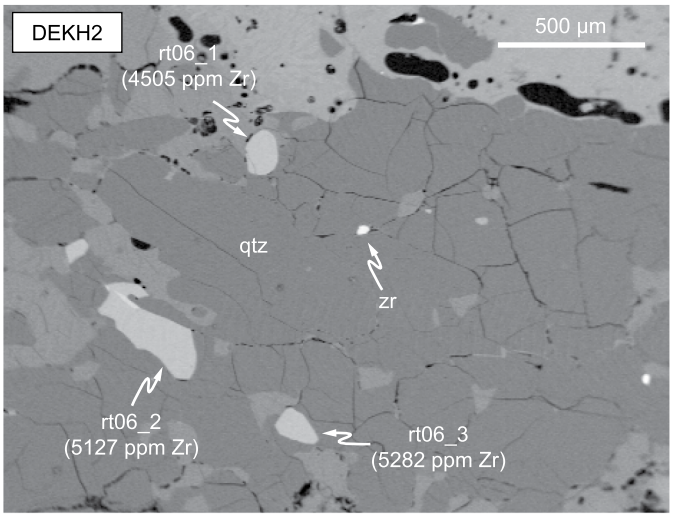

Extended Data Fig. 9 | BSE image showing example of Zr-in-rutile variation with proximity to zircon in sample DEKH2. Rutiles tend to have lower [Zr] when closer to zircon and higher [Zr] when isolated from zircon.